A Generalizable Lie Autoencoder for Emulating Barotropic Turbulence

I. Gorenstein[1], I. Wainer[1],C.B. Rocha[1],P.S. Peixoto[2]

[1]Instituto Oceanográfico, Universidade de São Paulo, Brazil
[2]Instituto de Matemática e Estatística, Universidade de São Paulo, Brazil

Key Points:

- Physics-Informed Autoencoder for Computational Fluid Dynamcis: A generalizable shallow-water emulator for the AB3-AM4 algorithm.
- Turbulence Emulation: High-fidelity simulation of barotropic turbulence via physics-informed autoencoders preserving physical quantities.
- Physics-Informed Latent Space: Nonlinear shallow-water solver via linear regression over a latent space of nonlinear observables.

This paper is a non-peer reviewed preprint submitted to EarthArXiv. This version has also been submited for peer review to the Journal of Advances in Modeling Earth Systems (JAMES)

Corresponding author: Iuri Gorenstein, `iuri.gorenstein@usp.br`

Abstract

Numerical ocean models rely on the discretization of primitive equations to simulate ocean dynamics, but their computational cost increases drastically with resolution. As an alternative, recent advances in neural networks (NN) have demonstrated promising applications in climate science, offering orders-of-magnitude faster simulations than traditional models through data-driven algorithms that can be continuously improved with observational data training. However, NN-based approaches for ocean modeling face critical challenges, including stability, physical consistency, and generalizability. This study presents a novel approach to embedding the barotropic dynamics of the Coastal and Regional Ocean COmmunity (CROCO) model, namely the AB3-AM4 algorithm, into a physics-informed NN. By leveraging a Lie auto-encoder, we transform the nonlinear barotropic dynamics into a latent space where they can be evolved using a linear operator. The network is tested on a linear idealized barotropic tsunami, as well as nonlinear geostrophic equilibrium and perturbation test cases. The results demonstrate stable evolution of surface height and barotropic velocities, conserving physical quantities, the expected energy spectra of the simulation and key eddy structures in turbulent flows. Furthermore, although it does not yet exhibit computational efficiency gains, the model is fully generalizable to any domain grid size and demonstrates comparable performance when applied to resolutions equal to or lower than those seen during training. This approach bridges the gap between traditional numerical models and NN algorithms, paving the way for hybrid modeling techniques that enhance ocean simulation beyond computational limitations.

Plain Language Summary

Recent advances in neural networks (NN) have demonstrated promising applications in climate science. In this work, we solve the shallow-water equations by introducing a novel model based on an NN autoencoder architecture. We evaluate our model using a benchmark suite of initial-value problems to assess its accuracy in preserving stability, turbulence, mass, and energy. Our results demonstrate that this architecture is highly promising for a wide range of fluid dynamics applications, effectively bridging the gap between neural networks and traditional numerical models.

1 Introduction

Fluid mechanics is the realm of physics equations that govern the dynamical evolution of any liquid or gas substance at any scale where Newton's laws are applicable. The ocean can be described as a fluid, which can be approximated by a set of primitive equations (Euler, 1752; Arakawa & Lamb, 1977; Randall, 2011). Numerical modeling discretizes these differential equations into a specific grid and uses them to evolve the ocean system in time (Döös et al., 2022). The discretizations are crafted to a set of possible parameters that assures the stability of the simulation, and to the desired approximation of the spatial and temporal derivative errors. Physical processes operating below the grid resolution are parameterized to ensure a closed system description. Low-resolution simulations underestimate the turbulence of real ocean dynamics. Creating realistic simulations requires high-resolution, state-of-the-art numerical models, demanding even larger and more efficient computers and data storage.

Neural networks programming takes a distinct approach to numerically simulating dynamical systems. In its simplest form, a neural network (NN) organizes part of the computer's memory into a set of layers. Starting from an input vector, each layer computes a linear combination of the values from the previous layer, followed by the application of a nonlinear activation function. This process is repeated through successive layers, ultimately producing an output. With a careful choice of training dataset, architecture, and loss function, any nonlinear problem can be approximated by an NN in a

data-driven approach (Haykin, 2009). In the last couple of years, breakthroughs in NN's architecture for climate data have been responsible for data-driven weather forecasting becoming a viable source of weather prediction (Pathak et al., 2022; Ben Bouallègue et al., 2024; Bi et al., 2023; Wang et al., 2024), while being orders of magnitude faster and more energy-efficient than traditional weather prediction models (Russkova, 2017). Simulating ocean dynamics is the next challenge of NN-powered climate models. However, filled with discontinuities, turbulent structures, and longer time steps, modeling the ocean can be more complicated than the atmosphere (Randall, 2011). Furthermore, the state-of-the-art NN models require extensive GPU resources, are physics-uninformed, and are unable to generalize outside their training domain. The latter two points raise a question that has been resonating inside the scientific community: "How can we trust the predictions of a data-driven climate model unable to generate long-term, realistic, and stable climate simulations?"

This study's objective is to develop an NN-powered ocean model informed by the Coastal and Regional Ocean COmmunity Model (CROCO - Auclair et al., 2024) and Koopman Theory (Azencot et al., 2020; Brunton et al., 2021), running on one GPU and trained to solve the nonlinear barotropic discrete equations of the AB3-AM4 algorithm (CROCO's barotropic algorithm). Generating stable simulations at any ocean domain, our model's applicability is the same as the traditional shallow-water model. This novel technique points to a direction where traditional numerical models and NN algorithms can be used together to create data-driven physics-informed models and study ocean circulation with a new perspective.

2 Data and Methods

2.1 Data

The training and test datasets used in this study were generated using the AB3-AM4 algorithm solver for the shallow water approximation (the barotropic mode of the CROCO model). Its code is available at the GitHub repository: https://github.com/IuriGorenstein/ShallowWaterEmulator (Gorenstein & Peixoto, 2026), togheter with all the code needed to train and apply the models in this study.

Two sets of problems were chosen to train and test the models (depicted in Table 1) representing the barotropic dinamics in two different regimes. This was necessary due to the lack of uniformity between the scales of the ocean circulation variables (sea surface height and horizontal velocities). The first training set is the Barotropic-Tsunami simulation on an abstract setting, used to see if the different models are able to reproduce the linear behaviours of the barotropic dynamics. An initial condition composed of a sea surface peack of 0.05 meter and nule horizontal velocities (First row in Table 2). This simulation has a total of 1400 time steps at a 100x100 pixel grid, with no Coriolis or advection forces, and with fixed spatial and temporal resolutions (Δx of 0.5 meter and Δt of 0.1 second), periodic borders, and gravity equals 1 m/s.

Following the test example from (Peixoto & Schreiber, 2019), the second training set is the geostrophic equilibrium and perturbation simulations. Composed by a 4800 time steps at a 200x200 pixel grid, with an homogenous Coriolis forces (2Ω), advection term, fixed spatial and temporal resolutions (Δx of 32 kilometer and Δt of 360 second), periodic borders, and gravity equals 9.81 m/s. This test example is ideal for testing our circulation models with a static initial condition of geostrific equilibrium and nonlinear dynamics. We validate our emulator in this turbulent flow simulation using Fourier spectrum analysis.

2.2 Methods

2.2.1 The primitive equations under barotropic approximation

In fluid mechanics, the barotropic approximation assumes that density depends only on pressure. Since pressure depends only on the vertical coordinate, horizontal pressure gradients arise solely from variations in the surface height. Consequently, at all depths, the pressure gradient force is uniform, causing the entire water column to move nearly in unison. This approximation is commonly used in shallow water equations and as a fast computational step in split-mode ocean circulation models, where it accounts for the influence of water column pressure on the mean flow. In ocean modeling, the thin shell approximation refers to the shallow water equations combined with geometric assumptions about the Earth's curvature, which simplifies large-scale ocean dynamics (Randall, 2011).

Let $\vec{u}_i = (u, v)$ denote the horizontal velocity field, g the gravitational acceleration, and f the Coriolis parameter, p the pressure and $\nabla_i = (\partial_x, \partial_y)$. The vertical coordinate z is oriented upward, with the ocean bottom at $z_{bottom} = -H(x, y)$, the free surface at $z_{surface} = \zeta(x, y, t)$ and column thickness is defined as $D(x, y, t) = H(x, y) + \zeta(x, y, t)$. Under the hydrostatic approximation ($\partial_z p = -\rho g$), integrating the continuity equation ($\partial_x u + \partial_y v + \partial_z w = 0$) and the Navier–Stokes equation ($\partial_t \vec{u}_i + \nabla_i(\vec{u}_i \otimes \vec{u}_i) + f\vec{k} \times \vec{u}_i = -\frac{1}{\rho_0}\nabla_i p$, discarding the stress, viscosity, and other external forces) in the water column under the incompressible fluid approximation ($\rho = \rho_0 = constant$) yields a set of three primitive equations (here neglecting temperature, and salinity variations). These equations describe the large–scale dynamics of the barotropic ocean system (Lionst et al., 1992).

$$\partial_t \zeta + \partial_x(Du) + \partial_y(Dv) = 0, \tag{1}$$

$$\partial_t u + u\partial_x u + v\partial_y u - fv = -g\partial_x \zeta, \tag{2}$$

$$\partial_t v + u\partial_x v + v\partial_y v + fu = -g\partial_y \zeta. \tag{3}$$

2.2.2 Dynamical system modeling

The barotropic ocean system can be represented as a vector $x = \begin{pmatrix} \zeta(t) \\ u(t) \\ v(t) \end{pmatrix}$, where ζ (the ocean surface height), u and v (the barotropic velocities) are two-dimensional scalar fields depending on the continuous time t. Its dynamics are described by $\frac{dx}{dt} = f(x, t)$. The function $f : \mathbb{R}^n \times \mathbb{R} \to \mathbb{R}^n$, where n is the total number of spatial degrees of freedom, consists of the nonlinear partial differential equations described in the previous section.

Dividing time into segments of equal length (Δt) and fixing τ, an integer number of these segments, our system's trajectory is well defined by a set of initial conditions ($x(t_0)$):

$$x(t_0 + \tau) = F^\tau(x(t_0)) = x(t_0) + \int_{t_0}^{t_0+\tau} f(x, t)dt \tag{4}$$

To create a simulation, we have access to measurement data of our modeled system, discretely sampled in time, on a specific grid. We use a finite difference scheme to approximate the differential equations and evolve the dynamical system.

2.2.3 The Regional Ocean Modeling System (ROMS) barotropic mode (AB3-AM4 algorithm)

The CROCO model with the Boussinesq approximation is a split-explicit regional ocean model that solves the primitive equations of fluid mechanics in a two-step finite-difference integration on a discrete C-grid with the same Fortran base code as the Regional Ocean Modeling System (ROMS) (Auclair et al., 2024). By default, for each baroclinic step, the model integrates about 60 barotropic steps to advance the ocean surface height and barotropic momentum.

The barotropic algorithm used by CROCO is the third-order Adams-Bashforth, fourth-order Adams–Moulton algorithm (AB3-AM4), a modified forward-backward algorithm with higher stability than other numerical models (Shchepetkin & McWilliams, 2009; Soufflet et al., 2016). The AB3 algorithm evolves the surface height (ζ) using the barotropic variables from times m, $m-1$, $m-2$ in a three-step algorithm to compute the future time $m+1$. The discretization of the AB3-AM4 integration steps follows.

$$\begin{pmatrix}\zeta\\u\\v\end{pmatrix}^{m+\frac{1}{2}} = \left(\frac{3}{2}+\beta\right)\begin{pmatrix}\zeta\\u\\v\end{pmatrix}^{m} - \left(\frac{1}{2}+2\beta\right)\begin{pmatrix}\zeta\\u\\v\end{pmatrix}^{m-1} + \beta\begin{pmatrix}\zeta\\u\\v\end{pmatrix}^{m-2}. \tag{5}$$

$$\zeta^{m+1} = \zeta^{m} + \Delta t\partial_x(D^{m+\frac{1}{2}}\ u^{m+\frac{1}{2}}) + \Delta t\partial_y(D^{m+\frac{1}{2}}\ v^{m+\frac{1}{2}}) \tag{6}$$

To not overwhelm the reader with notation, the partial derivative is maintained in its continuous form; however, to define its discrete meaning, its implementation on a quantity q at grid point i,j using a forward scheme is: $\partial_x q_{i,j} = \frac{q_{i+1,j}-q_{i,j}}{\Delta x}$ and $\partial_y q_{i,j} = \frac{q_{i,j+1}-q_{i,j}}{\Delta y}$. Equation (6) contains an explicit linear dependency where $\zeta^{m+1} = \zeta^{m} +$ Increment, leaving all the nonlinearity of the surface height integration in the increment part. β is a constant defining the temporal balance of the integration step, and $D^m = h + \zeta^m$ is the discrete column thickness.

After the AB3, the AM4 updates the barotropic velocities (u and v).The AM4 algorithm is modular to allow parallel computing and improved efficiency. The flux computation, here represented with the pressure gradient ($\partial_i D'$), the Coriolis contribution to the momentum term ($Cor_u = D^{m+\frac{1}{2}} fk\times u_i^{m+\frac{1}{2}}$), and the advection scheme ($Adv_{u/v} = u_i^{m+\frac{1}{2}}\partial_i u_i^{m+\frac{1}{2}} + u_j^{m+\frac{1}{2}}\partial_j u_i^{m+\frac{1}{2}}$, with $\{i,j\} = \{x,y\}$ or $\{y,x\}$) (Holland & Lin, 1975; Arakawa & Lamb, 1977; Shchepetkin & McWilliams, 2009). This integration step can also contain other parameterizations such as the stress or viscosity schemes (Auclair et al., 2024).

Using the cited modules, the AM4 integration step becomes:

$$D^{m+1}u^{m+1} = D^m u^m - \Delta t[g\partial_x(D'^2) - Cor_u + Adv_u] \tag{7}$$
$$D^{m+1}v^{m+1} = D^m v^m - \Delta t[g\partial_y(D'^2) - Cor_v + Adv_v] \tag{8}$$

Where $D' = H+\zeta'$ and $\zeta' = \delta\zeta^{m+1}+(1-\delta-\gamma-\epsilon)\zeta^m+\gamma\zeta^{m-1}+\epsilon\zeta^{m-2}$ is a temporal mean of the surface height using the newly computed values from the AB3 step; and the constants β,ϵ,γ, and δ are used to adjust the order of the time integration in the finite differences scheme, usually set to produce maximum stability of the model (Shchepetkin & McWilliams, 2009).

The linear relation in equations (7) and (8) is not explicit in u as the algorithm is designed to conserve the mass and momentum of the system. However, in the viewpoint of moment fluxes $U_i^m = D^m\vec{u}_i^m$, we can rewrite equations (7) and (8) as:
$\vec{U}_i^{m+1} = \vec{U}_i^m +$ Increment. Defining our system's evolution in time once again as the previous state plus a nonlinear increment.

These equations are discrete approximations from the continuous barotropic equations (1) to (3), extracted from the explicit AB3-AM4 implementation on the discrete C-grid in CROCO's Fortran code (Jullien et al., 2025). To improve this study's reproducibility and facilitate the NN coupling with the traditional shallow water model, we have translated this algorithm to Python (Gorenstein & Peixoto, 2026) using the exact same spatial discretization and time integration as the regional model.

If we choose the spatial derivatives in eqs. (6),(7) and (8) carefully, total energy is conserved to machine precision, making this a Hamiltonian system (Morrison, 1998; Bertalan et al., 2019). In this framework, we will recreate the AB3-AM4 algorithm dynamics generator as a linear operator (a.k.a Lie Operator) using neural networks and Koopman theory to produce a shallow water emulator (Olver, 1993).

2.2.4 Koopman theory

As mentioned before, the classic theory of dynamical systems usually involves solving PDEs in the form $\frac{dx}{dt} = f(x,t)$, where f is a nonlinear function. In Koopman theory, however, a transformation function $g : \mathbb{R}^n \rightarrow \mathbb{R}^m$ (with $m > n$), called the set of all possible observations of system $x \in \mathbb{R}^n$, is used to bypass the nonlinearities of the original PDEs, creating a new higher-dimensional space where the system can evolve linearly. From equation (4), the dynamical system evolves in its original space with $x_{t_0+\tau} = F^\tau(x_0)$. While in Koopman space, the same system evolves as $g(x_{t_0+\tau}) = g(F^\tau(x_0)) = \mathcal{K}^\tau g(x_0)$, with linear K (Koopman operator). Furthermore, we can explicitly find the time derivative of our system in Koopman space:

$$\mathcal{L}g(x_t) = \frac{dg(x_t)}{dt} = \lim_{\tau \to 0} \frac{g(x_{t+\tau}) - g(x_t)}{\tau} = \lim_{\tau \to 0} \frac{\mathcal{K}^\tau g(x_t) - g(x_t)}{\tau}. \tag{9}$$

This derivative operator $\mathcal{L}$ is the generator of the system's dynamics in the Koopman space, the Lie Operator. In this space, we can construct a linear base (φ) of independent eigenvectors (φ_n) of $\mathcal{K}$ with eigenvalues λ_n. For each φ_n, we have that $\mathcal{K}\varphi_n = \lambda\varphi_n$. From equation (9), we show that $\mathcal{L}$ and $\mathcal{K}$ share the same eigenvectors:

$$\begin{aligned} \mathcal{L}\varphi_n &= \lim_{\tau \to 0} \frac{\mathcal{K}^\tau \varphi_n - \varphi_n}{\tau} = \lim_{\tau \to 0} \frac{(\lambda^\tau - 1)}{\tau} \varphi_n, \\ \mathcal{L}\varphi_n &= log(\lambda)\varphi_n. \end{aligned}$$

The Koopman operator is guaranteed to exist for any dynamical system (Koopman, 1931; Koopman & Neumann, 1932; Brunton et al., 2021). Exchanging higher dimensionality to utilize linear algebra tools for nonlinear problems is the primary motivation behind the practical applications of Koopman theory. However, the Koopman space is, a priori, of infinite dimension, and the transformation g of all possible observations is usually very difficult to find explicitly (Brunton et al., 2021). Therefore, the key is to search for a finite-dimensional hyperplane in Koopman Space where we can approximate the Koopman operator $K : \mathbb{R}^m \rightarrow \mathbb{R}^m$, with $\infty > m > n$. This approach has yielded numerous results in dynamical systems modeling across various fields, including fluid mechanics (Schmid, 2010; Bagheri, 2013; Sharma et al., 2016; Herrmann et al., 2021).

2.2.5 Dynamical Mode Decomposition (DMD)

The Dynamical Mode Decomposition (DMD) is a machine-learning technique used to retrieve the finite-dimensional Koopman Operator (Brunton et al., 2021). Considering $X_t = [x_t, x_{t+1}, ..., x_{t+n}]$, a matrix containing multiple time steps of our system, and $X_{t+1} = [x_{t+1}, x_{t+2}, ..., x_{t+n+1}]$, a matrix containing our system one step forward in time,

we define K (the finite dimensional Koopman Operator) a linear term which controls the dependence of X_{t+1} on the previous state X_t. Our simplified problem can be described as:

$$X_{t+1} = K * X_t.$$

Where,

$$K = min_K\{X_{t+1} - KX_t\} = X_{t+1}X_t^T.$$

Different variations of DMD can be used to perceive the operators that better represent the dynamical operator of the system. For example, DMD with Control (DMDc) separates the linear and nonlinear terms of the system's dynamics. Furthermore, Extended DMD (e-DMD) describes the system using a matrix with additional nonlinear measurements. Once again, we want to find the correct measurements that increase our system's dimensionality enough, permitting us to evolve its dynamics using a linear operator. Considering $G(X_t) = [[x_t, g_1(x_t), g_2(x_t)], [x_{t+1}, g_1(x_{t+1}), g_2(x_{t+1})], ..., [x_{t+n}, g_1(x_{t+n}), g_2(x_{t+n})]]$, where the functions g represents the additional measurments of my system in time (analogous to the $g(x)$ from Section 2.2.4). The problem can be described in terms of a linear operator K that approximates the Koopman Operator in this high dimensional finite space:

$$G(X_{t+1}) = K * G(X_t)$$

Rewriting the Koopman operator as $K = L + I$, we can redefine our problem as follows:

$$G(X_{t+1}) = K * G(X_t) = (L + I) * G(X_t) \tag{10}$$
$$L * G(X_t) = K * G(X_t) - G(X_t) \tag{11}$$

Assuming the Koopman operator $\mathcal{K}$ from the system approximates the finite-time evolution operator K over one time step, then $L = K - I$ is a first-order discrete approximation of the continuous Lie operator as defined by eq. (9).

2.2.6 Lie Auto-Encoder (LieAE)

An autoencoder (AE) is a neural network architecture that transforms the state space from an input vector into another (i.e., a latent space) via an encoder and back to the initial space via a decoder. In Azencot et al. ((2020)), a consistent Koopman AE with a simple architecture was applied to a set of nonlinear physical problems, including fluid advection. Here, we will do a similar application, computing the Lie Operator in a more generalizable local setup than Azencot.

Figure 1 illustrates the straightforward information flow designed for computing the increments of the AB3-AM4 algorithm with the LieAE. Each pixel of our system, $x_t = x(\zeta_t, u_t, v_t)$, is individually encoded at time t using g_e (a shallow forward network with ReLU6 function). In the network's latent space, a linear operator $\mathcal{L}$ is applied to compute the increment of that time step forward in time. After this, we decode the dynamical increment back to the initial space using g_d and then advance the system forward. In practice, we seek encoders g_e and g_d and operator $\mathcal{L}$ such that:

$$g_d \circ \mathcal{L} \circ g_e\{x_t\} = x_{t+1} - x_t, \tag{12}$$

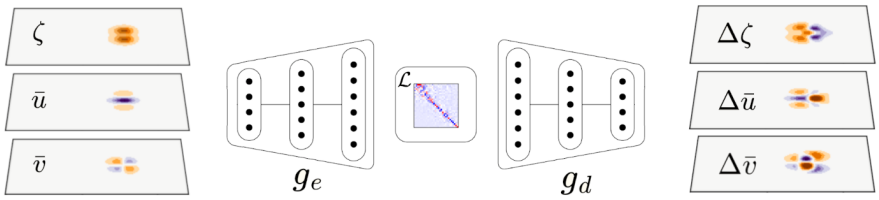

Figure 1. Lie AE illustration. Data representing a 2D barotropic ocean system with color representing sea surface height (ζ) and barotropic velocity (u, v). From left to right: the input data is encoded to the Koopman space (g_e). The Lie operator ($\mathcal{L}$), representing the dynamics of the system in the latent high-dimensional Koopman space, is used to compute the increment of the system. The decoder (g_d) takes the system back to the input space, recovering the system's increment ($\Delta\zeta$,Δu, and Δv). Adapted from Azencot et al. (2020)

By training $\mathcal{L}$ to recover the system increment via nonlinear encoding and decoding, we aim to create a discrete generator of the AB3-AM4 dynamics in latent space. Assuming the Koopman operator $\mathcal{K}$ from the system approximates the finite-time evolution operator $\mathcal{K}^1$ over one time step $\tau = 1$, then, the increment in the network's latent space can be written as: $\mathcal{L} \circ g_e\{x_t\} \approx \mathcal{K}^1 \circ g_e\{x_t\} - g_e\{x_t\}$. Where the learned $\mathcal{L} \approx \mathcal{K}^1 - I$ is the first-order discrete approximation of the continuous Lie operator we defined before, analogous to the L operator from e-DMD.

2.2.7 Loss functions

The loss functions used in the LieAE's training guarantee that the individual pieces of the network are consistent with the previous description. Following Azencot et al. ((2020)), we use the identity loss (ε_{id}): the difference between encoding and deconding our system trought the network and the original system (with no linear operator being used in the latent space); The forward loss (ε_{fwd}): the difference between the truth and the network's prevision of the system evolved forward in time (calculating the system increment with the $\mathcal{L}$ operator in the latent space).

$$\varepsilon_{id} = \frac{1}{2n} \sum_{t=1}^{n} ||x_t - \hat{x}_t||^2, \tag{13}$$

$$\varepsilon_{fwd} = \frac{1}{2n} \sum_{t=1}^{n} ||x_{t+1} - \hat{x}_{t+1}||^2, \tag{14}$$

In equations (13) and (14), x_t refers to the true system at time t and $\hat{x}_t$ refers to the network's prediction.

2.2.8 Input Vectors

The input vectors have 30 dimensions for evolving ζ and 60 dimensions for u or v. They consist of variables needed for the AB3-AM4 algorithm to evolve each pixel one step in time, therefore, they are given to the models to do the same. For evolving a $\zeta_{i,j}$ pixel at any grid point, these variables are: $\zeta_{i,j}, \zeta_{i\pm1,j}, \zeta_{i,j\pm1}, u_{i,j}, v_{i,j}, u_{i,j-1}, v_{i-1,j}$,topography, dx, dy and dt at times $t, t-1, t-2$. For evolving the horizontal velocities pixels, we need in addition to the previous variables: $\zeta_{i\pm1,j\pm1}, u_{i-1,j}, u_{i+1,j-1}, v_{i,j-1}, v_{i-1,j+1}$ at times $t, t-1, t-2$ and the ζ variable prediction at time $t+1$.

2.2.9 Physics-Informed Pre-Encoder Architecture

To construct the input vector described above efficiently, the initial encoder layers are informed by the AB3-AM4 algorithm. These layers include an initial 2D convolution with fixed weights that retrieves the required variables at neighboring grid points (Fig. 2); a learnable parameter that combines different time levels for each variable, emulating the β parameter in Eq. (5); and linear and bilinear layers without activation functions, which compute spatial averages of the barotropic variables to shift ζ, u, and v between locations on the C-grid and form the corresponding spatial derivatives (∂_x and ∂_y). This architecture provides nonlinear pathways for known combinations of the shallow-water variables, allowing the network to construct a richer variable representation. The pre-encoder acts as a simple attention mechanism by generating nonlinear combinations of the inputs, thereby allowing the network to explore higher-dimensional representations and cross-variable dependencies (Jayakumar et al., 2020). Recent studies have employed similar neural-physics techniques to improve the computational efficiency of traditional finite-difference algorithms on GPUs and TPUs (Zhao et al., 2020; Chen et al., 2026). From a Koopman perspective, the pre-encoder augments the original state space with nonlinear observables of the system variables, as described in the preceding DMD section. It therefore provides physics-based guidance by supplying transformations analogous to those used by the AB3-AM4 algorithm. Without this physics-informed encoder, the network failed to generalize beyond its training dataset (not shown). An analogous pre-encoder architecture processes the input to the MLP model.

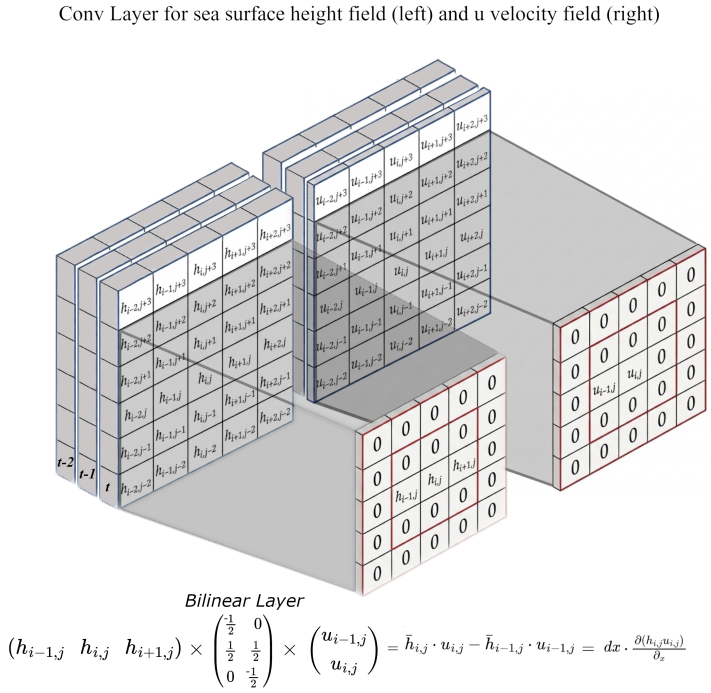

Figure 2. Simplified schematic of the physics-informed pre-encoder. The ζ and u fields are partially shown. Lined up in times t, t-1 and t-2, with a 5 × 5 convolutional kernel applied to each field to sample the required grid points. The weights of a bilinear layer are illustrated as a 2 × 3 matrix, multiplying the convolutions' output to produce the corresponding spatial derivative.

3 Results

First, to train and test our models in a linear setting, we use a barotropic tsunami case test, defined by a cosine bell shaped peak (Table 2 - Initial Condition) and continuity accross the edges of a periodic domain without coriolis or advection forces in a square domain of 100x100 pixel C-grid scheme. Standard Mean Squared Error (MSE) metrics are used to compare the models' acuracy in training (Table 1). Our models are pixel oriented, therefore, we only use 60 time steps from 100 random pixels in our domain to train the models. Using the full domain, 1400 time steps are used to test our model (Table 2). To analyse if the different model's produced longterm stable simulations, we measure the conservation of physical properties (mass, momentum and energy) during the simulations (Figure 3). Finally, we train and test our models with a geostrophic balanced initial condition, where the coriolis, advection and pressure gradient forces even out and we expect the system to stay constant (Figure 4). The same initial condition with a small perturbation is used to explore the model's hability in reproducing nonlinear dynamics (Tabela 4). This setup causes non linearities to arise from the coriolis and advection terms, resulting in a turbulent flow with vortices (Peixoto & Schreiber, 2019).

Linear Problem (Barotropic Tsunami)

Model Description and Training

The machine learning models used to embed the barotropic ocean dynamics of the AB3-AM4 algorithm are displayed in Table 1. The training of the networks was made using Adam Optimizer and the Loss functions previously described (see Methods).

Time steps 260-320 were used for training, while steps 400-460 were used for cross-validation. Different sizes of layers were tested for each NN; here we present only the networks that accomplished the best results. The input vectors contain the system present, past and paster state, the constants used in the definition of domain and forces applied, and the respective neighbouring variables needed to integrate the Navier Stokes equations as described in the Methods section. All models used the same input vectors to evolve the system. The training was executed for 400 epochs with an initial learning rate of 0.001 and a learning rate decay of 0.6 every 4 non-improving epochs using pytorch's scheduler. To avoid overfitting, dropout layers and early stopping were implemented. The evolution of the loss function during training is shown for each network in the 'Training' column of Table 1. The network's final cross-validation forward loss score can be viewed in the last column of Table 1. Since this initial condition and system constants hold abstract carefully choosen values, including gravity constant equals to 1, no normalization was needed to train the networks.

Model	Architecture	Layers	Training	Validation Loss Forward
DMD control	$X_{t+1} = X_t + BY_t$	————	$\arg\min_B \|\|\Delta X_{t+1} - BY_t\|\|_F$	$1.665e{-}18$
LieAE	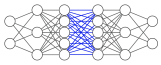	AE: 3 dense layers, 128 neurons each with $ReLU6$ function. Latent space: 20 neuron dense layer	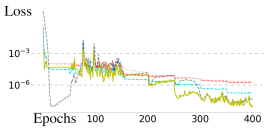	$1.835e{-}08$
MLP		3 dense layers, 100 neurons each, with $ReLU6$ function	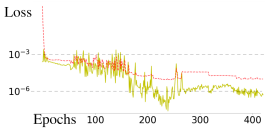	$9.672e{-}09$

Table 1: The data-driven models used in this study. From top to bottom: The Dynamical Mode Decomposition with control (DMDc), The Lie Auto-encoder (LieAE), and the Multi-layer Perceptron (MLP). From left to right: The models' architecture, with black edges symbolizing connections with non-linear activation functions ($ReLU6$), while blue connections symbolize a linear layer with no activation function; The layers description (for the NN); The dynamical solver linearity; The training algorithm for DMDc and loss function curve during network training: Blue/red, magenta/black for 100/240 step mean losses of the forward and identity functions, respectively, while yellow is for the cross-validation loss forward.

Model Validation

The barotropic tsunami test case steps 0, 200, 600, 1000, and 1400 of the surface height are displayed in Table 2, along with their final biases. The video of the complete simulations is also available in the Supplementary Material.

Figure 3 contains the evolution of the model's physical properties: Total mass ($D = H + \zeta$, blue curve from Figure 3 - 'a') and Potential Energy ($\frac{g(H+\zeta)^2}{2}$, bold line from

Figure 3 - 'b') compared to the original AB3-AM4 simulation (dashed line from Figure's 3 - 'b').

The behaviour of DMDc is precisely equal to the original AB3-AM4 algorithm, as we can see by the cross-validation error below the numerical precision of double-precision floating point (Table 1 final column), the absence of bias in Step 1400 (Table 2), and the overlapping of potential energy with the "truth" simulation Step 1400 (Table 2). This result illustrates both how straightforward Koopman theory can be in such idealized settings (Brunton et al., 2016, 2021) and how effectively the pre-encoder reproduces the AB3-AM4 derivative calculations in a GPU-friendly framework (Chen et al., 2026). When the PDEs being integrated are already discrete and known, the observables $g(x)$ needed to evolve the controled system (DMD control's Architecture column in Talbe 1) using a linear operator are well defined. This makes the task of identifying the local Lie operator relatively trivial, since it acts on a set of physically meaningful, explicitly defined variables. In these cases, the value of Koopman theory lies less in discovering the right observables and more in unravelling the AB3-AM4 algorithm code with an ML approach, leveraging the linear structure of the dynamics for analysis and potential control.

The simulation produced by the LieAE exhibits a positive surface height bias relative to the reference "truth" provided by the AB3-AM4 simulation, one order of magnitude smaller than the main wave propagating. This anomaly appears at the center of the domain, where the initial condition sets the surface height peak. As shown in Figure 3 'b', the potential energy jumps at the first 200 steps of the simulation, after which the simulation stabilizes. This may be reflecting a difficulty of generalizing in extreme, unseen or low sampled conditions, such as the tsunami's initial condition.

The simulation generated by the Multi-layer Perceptron (MLP) model is shown in the bottom row of Table 2, and the evolution from its total surface height and potential energy is depicted in Figure 3 'c'. The network shows a positive drift concerning the AB3-AM4 algorithm, indicating that, although its cross-validation loss was smaller than the LieAE ($9.672e{-}09$ against $1.835e{-}08$, respectively), it is not as stable as the physics-informed network.

Model	Initial Condition	Step 200	Step 600	Step 1000	Step 1400	Step 1400 - BIAS
AB3-AM4 (TRUTH)	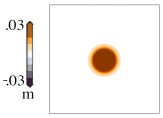					————
DMDc	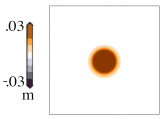					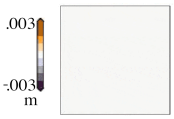
LieAE	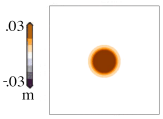					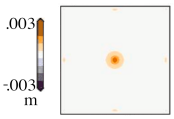
MLP	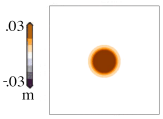					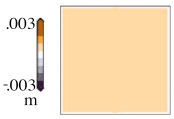

Table 2: Model validation on the test dataset (The barotropic tsunami test case). From top to bottom: the AB3-AM4 simulation (Truth); the Dynamical mode decomposition with control (DMDc); The Lie Auto-encoder (LieAE); The Multilayer Perceptron (MLP). From left to right: the Initial Condition, followed by steps 200, 600, 1000, 1400 from each simulation. All simulation step figures use the same colorbar, ranging from 0.03 to -0.03 meters. In the final column, the final Bias from each model simulation is compared with the Truth using a colorbar ranging from 0.003 to -0.003 meters.

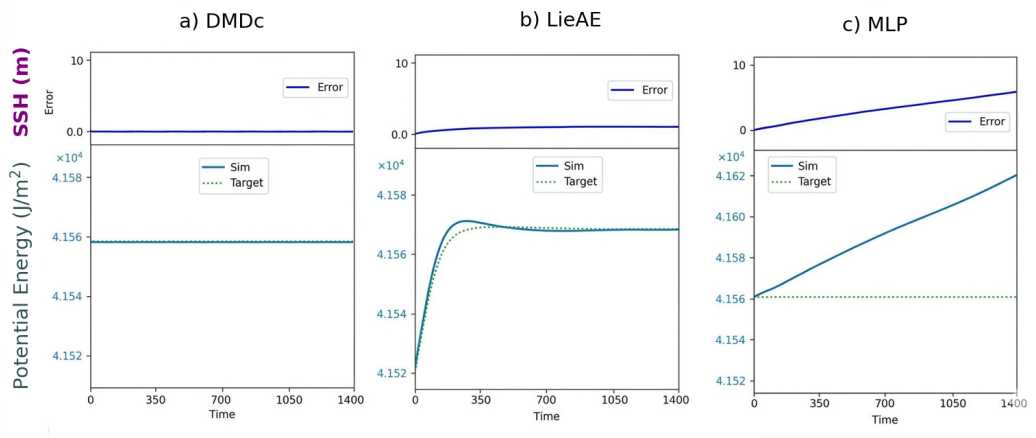

Figure 3. Plot of physical properties during the tsunami test case simulation. (a) the Dynamical Mode Decomposition with control (DMDc); (b) the Lie AutoEncoder (AE); (c) the Multi-Layer Perceptron (MLP). At the top, the sea surface height (ζ) error is in blue. At the bottom, the Potential Energy (J/m^2) in bold line for the respective model simulation, and dashed line for the target CROCO simulation (true AB3-AM4 algorithm).

Nonlinear Problems (Geostrophic Balance and Perturbation)

To study how the model performs in an equilibrium and perturbed nonlinear regimes, we retrained the models with Geostrific Balance and Perturbation simulations. These setups are described in great detail by (Peixoto & Schreiber, 2019). They consist of a 2D domain with a constant Coriolis force and periodic boundaries (2D Torus). The initial condition is in equilibrium between the pressure gradient, coriolis and advection forces. Furthermore, if we add a small perturbation to this initial condition, we force our system out of its equilibrium state, generating a turbulent flow.

Model Description and Training

The models' architectures are the same shown in Table 1 and the training was made using Adam Optimizer and the Loss functions as described in the previous sections. However, since the initial condition for the nonlinear problems have ζ ranging from 0 to 1.500 meters and horizontal velocities from -40 to 40 km/h, the network is retrained for the batch normalization layers to adjust to the new intervals, together with the output vectors' normalization using the mean and standard deviation of the new training set. This procedure forces the training set targets to have zero mean and standard deviation equals one. Although this is necessary to avoid saturation of the Encoder and Decoder layers, it also signifies a high chance of low generalizability for the system's states ranging outside this training dataset. Furthermore, the training consisted of time steps 3000 to 3300 of the Geostrophic Equilibrium with perturbed initial condition simulation. To speed up the training process, a mask that selects six hundred random pixels from the 200x200 pixel domain was applied to train and cross validate the networks on small batches. The training was implemented for 100 epochs and took around two hours (not shown).

Model Validation

The geostrophic equilibrium initial condition (Fig. 4) is evolved for the duration of 86400 seconds (one day) using the AB3-AM4 algorithm and the Lie AE using different spatial and temporal resolutions. Since the condition has an analytical solution of equilibrium, we can check the error of each model by comparing the final state to the initial condition. The final scores are shown in Table 3.

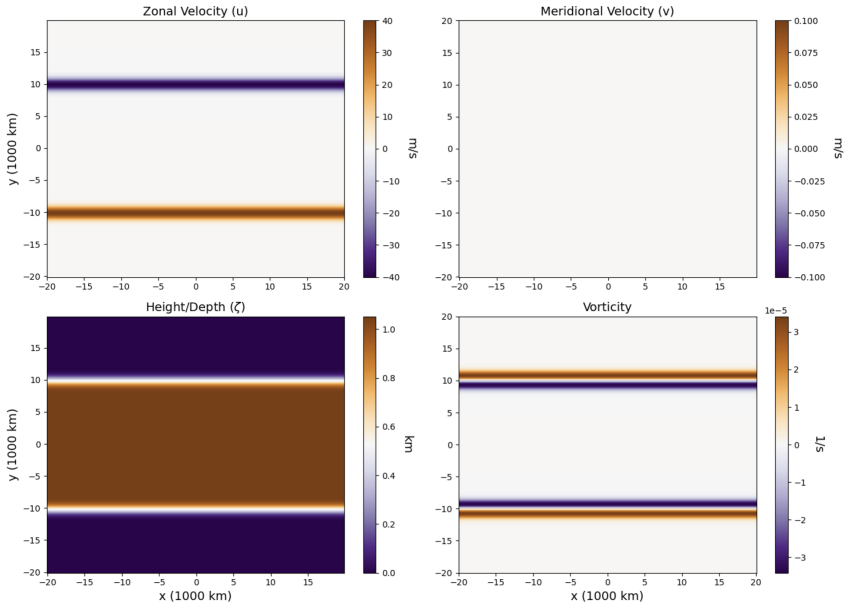

Figure 4. The Geostrophic Equilibrium Initial Condition. Top left: the u velocity field. Top right: the v velocity field. Bottom left ζ field. Bottom right: vorticity field.

Model	Spatial resolution grid	Dt (min)	U error	V error	Zeta error	Integration time (s)
AB3-AM4	50x50	24.0	0.14487	0.13490	24.4954	0.104
Lie AE	50x50	24.0	0.38829	0.13914	24.2755	0.627
AB3-AM4	100x100	12.0	0.05591	0.07491	6.13998	0.225
Lie AE	100x100	12.0	0.27575	0.06052	7.41681	1.274
AB3-AM4*	200x200	6.0	0.01465	0.02782	1.58342	1.477
Lie AE*	200x200	6.0	0.18029	0.04789	6.88767	4.611
AB3-AM4	400x400	3.0	0.00379	0.00693	0.39472	16.347
Lie AE	400x400	3.0	0.25093	0.10210	5.13011	30.607

Table 3: The u, v, and ζ errors of the Lie AE and the AB3-AM4 algorithm at different resolutions. The domain's lenght is maintained fixed using earths radius ($L = 40,000km$) The asterisk marks the resolutions used for network training ($dx = \frac{L}{200}$ km and $dt = 6$ min).

The errors in the resolutions that were not used in the LieAE's training (without asterisk rows in Table 3) show the network's difficulty to fully generalize the AB3-AM4 problem outside the training parameters. Nevertheless, LieAE exhibits skills comparable to the AB3-AM4 algorithm for the Geostrophic Balanced problem at resolutions equal to or lower than the training data ($200x200$ grid and $Dt = 6$min).

The perturbed initial condition (Fig. 4 first column) is used to test the network's ability reproducing eddys and nonlinearity. The final frame (Fig. 4 last column) shows the sucess of the LieAE simulating longterm turbulent flows (4800 simulation steps).

Model	Initial Condition	Step 2400	Step 4800
AB3-AM4 (TRUTH)	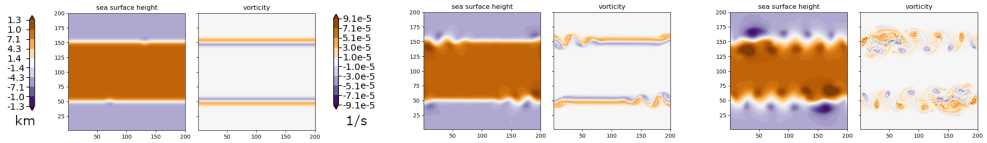		
LieAE	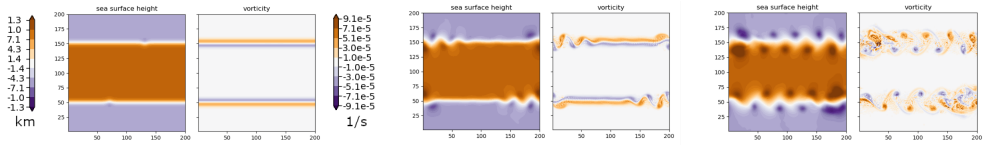		
Bias	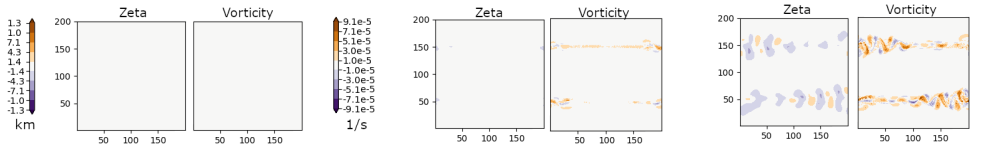		

Table 4: Model validation on the non-linear test dataset (The geostrofic equilibrium with initial perturbation). From top to bottom: the AB3-AM4 simulation (Truth); The Lie Auto-encoder (LieAE). From left to right: the Initial Condition, followed by steps 2400 and 4800 from each simulation. The simulation state is depicted by the sea surface height (Zeta) and vorticity snap shots. The figures use the same colorbar, ranging from -500 to 1300 meters (Zeta plots) and $-8 * 10^{-5}$ to $8 * 10^{-5}\ s^{-1}$ (vorticity plots). In the final row, the Bias between the simulations using the same colorbars for vorticity and from -1300 to 1300 meters for the Zeta variable.

The final state of each simulation is analysed through the lens of its kinetic energy spectra (Fig. 5). The analysis of the energy spectra is related to the study of turbulence in fluid dynamics models and is commonly used to validate simulations (Peixoto & Schreiber, 2019). While the LieAE accurately captured the overall AB3-AM4 energy spectra, it exhibited an overestimation of the energy content at shorter wavelengths (2×10^5) relative to the target simulation.

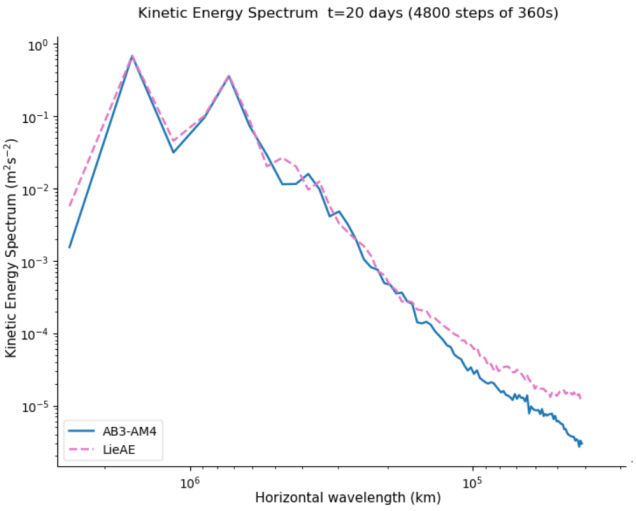

Figure 5. Kinetic energy spectrum from step 4800 of the simulation using the AB3-AM4 algorithm (bold line) and the LieAE (dashed line).

4 Discussion

Traditional numerical models offer several advantages for simulating ocean circulation. They solve discrete approximations of the governing differential equations, and benefit from well-established methods for validating their solutions against analytical benchmarks (Pond & Bryan, 1976; Fox-Kemper et al., 2019), eliminating spurious computational modes (Bryan, 1997), conserving physical quantities (Bryan, 1997), applying numerical filters for stability enhancement (Rosati & Miyakoda, 1988; Bryan, 1997), and performing stability analyses via characteristic polynomials (Higdon, 2006; Randall, 2011).

However, replacing the traditional model with NNs, regardless of architecture, offers two notable advantages: (i) A significant computational speedup when using large integration time steps, which traditional models cannot accommodate due to stability constraints such as the Courant–Friedrichs–Lewy (CFL) condition (Döös et al., 2022). Apart from the parallelization/GPU-friendly software, this scalability advantage is a key reason NNs can outperform conventional models in terms of computational efficiency (Russkova, 2017; Hu et al., 2022); (ii) NNs are inherently data-driven and can approximate any linear and nonlinear behaviors without explicit knowledge of the data-generating process. This feature allows them to downscale high-resolution simulations, also speeding up the computational process without losing the complex behaviour present in more fine structures. Furthermore, when fine-tuned with observations or non-trivially simulated data, they can implicitly parameterize sub-grid processes not explicitly resolved in the governing equations. Therefore, NNs can capture features that traditional models might overlook or simplify in their higher-level description of the discretized physical equations (Bucci, 2020; Hu et al., 2022).

Recent studies have explored the use of Neural Networks as pointwise shallow-water solvers. While Li and Feng employ physics-informed networks to solve nonlinear shallow water equations, their domain-specific architectures restrict generalization beyond the training set (Li et al., 2024; Feng et al., 2025). In contrast, Keppler et al. (2025) develop a generalized neural operator for flood emulation. However, their baseline scenarios, similar to our linear case problem, lack complex eddy dynamics, and the network struggles to capture nonlinear interactions when external forcings are introduced (Keppler et al., 2025). Furthermore, while broader data-driven operators have succeeded in sim-

ulating highly nonlinear dynamics, such as complex 3D baroclinic circulations (Bire et al., 2025), they inherently lack the physical interpretability of equation solvers. More broadly, although recent emulators have succeeded in simulating barotropic turbulence, the long-term preservation of fine-scale turbulent structures remains a well-documented challenge (Kontolati et al., 2024). Standard networks optimized primarily via Mean Squared Error (MSE) loss frequently suffer from spectral bias, tending to smooth out small-scale features over extended simulations. While our proposed framework does not target the massive computational speedups achieved by these previous data-driven models (advantage i), its lightweight architecture and pointwise equation-constrained generalizability provide a highly accurate and robust methodology for sustaining long-term turbulent dynamics, preserving small-scale turbulence.

As shown in Table 3 and the bias plots from Table 4, a model trained solely on a numerical algorithm as ground truth cannot surpass the inherent skill of that algorithm. Nevertheless, the neural network model runs efficiently on a single GPU and has created a data-driven parallelized longterm stable algorithm for simulating turbulent barotropic flows at diverse domains. A natural extension of this work could be the use of a LieAE to downscale turbulent flows; parametrizing high-resolution processes in low-resolution grids could provide a gain in skill and efficiency using this architecture. Furthermore, the pointwise LieAE architecture offers a key advantage. Leveraging Koopman operator theory, it provides a physics-informing latent space where the system's dynamics evolve linearly with simple matrix multiplication (Fig. S1 and S2 in Supplementary Material), enabling more interpretable analysis and potentially controlling complex nonlinear behavior (Brunton et al., 2017).

5 Conclusions

Building on established shallow-water algorithms and neural-physics approaches, we propose the Lie Auto-Encoder (LieAE) architecture for evolving the barotropic dynamics of fluid flows. As part of this work, we translated the Regional Ocean Modeling System's (ROMS) barotropic step, implemented using the AB3-AM4 algorithm, into Python and trained an autoencoder that maps the system state to a higher-dimensional latent-variable space, where a linear operator advances the dynamics. To evaluate our model in a linear setting, we use a barotropic tsunami test case defined by a cosine bell-shaped peak (Table 2 - Initial Condition). We train our model using explicit AB3-AM4 barotropic simulations, and compare the LieAE performance with the Dynamic Mode Decomposition with control (DMDc) and the Multi-Layer Perceptron (MLP) models. MSE metrics are used to compare model accuracy during training (Table 1), and for testing, we use a 1400-step simulation evolving the same initial condition (Table 2). Furthermore, we measure the conservation of mass and energy during the runs (Figure 3). Finally, we train and test the LieAE model using a geostrophically balanced initial condition with and without perturbation (Figure 4), exploring the model's ability to reproduce nonlinear dynamics (Table 4).

In the initial linear case, the physics-informed LieAE demonstrated greater stability than the MLP throughout the simulation (Figure 3). In the geostrophic balanced initial condition (Figure 4), the LieAE produced a long term stable simulation when using the resolution from the training dataset (200x200 spatial grid with dt=360s), conserving the barotropic variables equivalently as the AB3-AM4 algorithm (errors 4 orders of magnitude smaller than the initial condition). When testing the network with unseen resolutions, the network presents larger errors, demonstrating the failure to generalize outside its training resolution (Table 3 bottom row). Under perturbed initial conditions, the LieAE successfully replicated the nonlinearities of the AB3-AM4 algorithm, generating the expected eddy structures of the flow (Table 4). Although comparable, the final state (step 4800) of the simulation's energy spectra showed that more energy cascaded to smaller scales when using the LieAE model than the AB3-AM4 algorithm (Figure 5). This capacity to preserve energy at smaller scales represents a notable advantage over previous shallow water emulators, which frequently smooth out fine-scale structures during extended simulations (Li et al., 2024; Kontolati et al., 2024; Keppler et al., 2025).

Inspired by the consistent Koopman autoencoder framework proposed by Azencot et al. (2020), the LieAE when informed with the AB3-AM4 physics and interpretable architecture (see methods), generated stable dynamics for a range of shallow water examples, including nonlinear turbulent flows, at resolutions not higher than its training data-set. Although its integration time is not faster than the original AB3-AM4 algorithm, its potential use for downscaling, parallelization and possible improvement via fine tuning displays a number of possible next steps and applications for this new architecture, such as:

(I) Replacing CROCO's barotropic fast step with our neural network could provide a straightforward path to derive additional validation metrics and enable online training of the model. However, integrating Fortran-based numerical models with Python-based machine learning frameworks remains a significant challenge, and has been a major obstacle in recent efforts to combine traditional modeling with modern ML techniques (Ott et al., 2020; Zhong et al., 2023).

(II) Downscaling turbulent flows. If successful, this network could present a gain in efficiency (simulating turbulent flows in low dimensional grids) and allow a comparison between the different linear operators (fine-tuned and AB3-AM4-based) in its physically motivated latent space, creating a physics-informing tool for studying the network's parametrizations.

(III) Eddy detection (Kolář, 2007; Gao & Liu, 2018; Amran Abolholl et al., 2024). The LieAE can simulate stable vortices and its architecture may be modified and adapted to finding or predicting eddy paths.

(IV) Leveraging the network as a barotropic core for building a larger, physics-informed model could help replicate the split-explicit structure of CROCO using a fully data-driven architecture. This approach could bridge physical modeling and machine learning, yielding more realistic ocean simulations with explainable NNs (Jiang et al., 2021; Stier et al., 2024).

Open Research Section

Code and Data availability: The current version of the models used to produce the results in this paper, the discretized AB3-AM4 algorithm and Neural-Network's training functions with CUDA-pytorch engine are available at: "https://github.com/IuriGorenstein/ShallowWaterEmulator", as are scripts to produce the plots for all the simulations presented in this paper (Gorenstein & Peixoto, 2026).

Conflict of Interest disclosure

The authors declare there are no conflicts of interest for this manuscript.

Acknowledgments

This study was financed in part by the Coordenação de Aperfeiçoamento de Pessoal de Nível Superior - Brasil (CAPES) - Finance Code 001;

References

Amran Abolholl, H. A., Teschner, T.-R., & Moulitsas, I. (2024). A hybrid computer vision and machine learning approach for robust vortex core detection in fluid mechanics applications. *Journal of Computing and Information Science in Engineering*, *24*(6), 061002.

Arakawa, A., & Lamb, V. R. (1977). Computational design of the basic dynamical processes of the ucla general circulation model.

Auclair, F., Benshila, R., Capet, X., Debreu, L., Dumas, F., Jullien, S., & Marchesiello, P. (2024). Coastal and regional ocean community model (2.0). doi: https://doi.org/10.5281/zenodo.11036115

Azencot, O., Erichson, N. B., Lin, V., & Mahoney, M. (2020). Forecasting sequential data using consistent koopman autoencoders. In *International conference on machine learning* (pp. 475–485).

Bagheri, S. (2013). Koopman-mode decomposition of the cylinder wake. *Journal of Fluid Mechanics*, *726*, 596–623.

Ben Bouallègue, Z., Clare, M. C., Magnusson, L., Gascón, E., Maier-Gerber, M., Janoušek, M., ... others (2024). The rise of data-driven weather forecasting: A first statistical assessment of machine learning–based weather forecasts in an operational-like context. *Bulletin of the American Meteorological Society*, *105*(6), E864–E883.

Bertalan, T. S., Dietrich, F., Mezi'c, I., & Kevrekidis, I. (2019). On learning hamiltonian systems from data. *Chaos*, *29 12*, 121107. doi: 10.1063/1.5128231

Bi, K., Xie, L., Zhang, H., Chen, X., Gu, X., & Tian, Q. (2023). Accurate medium-range global weather forecasting with 3d neural networks. *Nature*, *619*(7970), 533–538.

Bire, S., Lütjens, B., Azizzadenesheli, K., Anandkumar, A., & Hill, C. (2025). Ocean emulation with fourier neural operators: Double gyre. *Journal of Advances in Modeling Earth Systems*, *17*(7), e2023MS004137.

Brunton, S. L., Brunton, B. W., Proctor, J. L., Kaiser, E., & Kutz, J. N. (2017). Chaos as an intermittently forced linear system. *Nature communications*, *8*(1), 19.

Brunton, S. L., Budišić, M., Kaiser, E., & Kutz, J. N. (2021). Modern koopman theory for dynamical systems. *arXiv preprint arXiv:2102.12086*.

Brunton, S. L., Proctor, J. L., & Kutz, J. N. (2016). Discovering governing equations from data by sparse identification of nonlinear dynamical systems. *Proceedings of the national academy of sciences*, *113*(15), 3932–3937.

Bryan, K. (1997). A numerical method for the study of the circulation of the world ocean. *Journal of Computational Physics*, *135*, 154-169. doi: 10.1006/JCPH.1997.5699

Bucci, A. (2020). Realized volatility forecasting with neural networks. *Journal of Financial Econometrics*. doi: 10.1093/JJFINEC/NBAA008

Chen, B., Heaney, C. E., & Pain, C. C. (2026). Neural physics: Using ai libraries to develop physics-based solvers for incompressible computational fluid dynamics. *Computers & Fluids*, 106981.

Döös, K., Lundberg, P., & Campino, A. A. (2022). *Basic numerical methods in meteorology and oceanography*. Stockholm University Press.

Euler, L. (1752). Découverte d'un nouveau principe de mécanique. *Mémoires de l'académie des sciences de Berlin*, 185–217.

Feng, D., Tan, Z., Lin, Z., Xu, D., Yu, C.-W., & He, Q. (2025). A comparative study of physics-informed and data-driven neural networks for compound flood simulation at river-ocean interfaces: A case study of hurricane irene. *Journal of Geophysical Research: Machine Learning and Computation*, *2*(4), e2025JH000758.

Fox-Kemper, B., Adcroft, A., Böning, C., Chassignet, E., Curchitser, E., Danabasoglu, G., ... Yeager, S. (2019). Challenges and prospects in ocean circulation

models. *Frontiers in Marine Science*. doi: 10.3389/fmars.2019.00065

Gao, Y., & Liu, C. (2018). Rortex and comparison with eigenvalue-based vortex identification criteria. *Physics of Fluids*. doi: 10.1063/1.5040112

Gorenstein, I., & Peixoto, P. (2026, May). *Shallowwateremulator.* Zenodo. Retrieved from `https://github.com/IuriGorenstein/ShallowWaterEmulator` doi: 10.5281/zenodo.XXXXXXXX

Haykin, S. (2009). *Neural networks and learning machines, 3/e*. Pearson Education India.

Herrmann, B., Baddoo, P. J., Semaan, R., Brunton, S. L., & McKeon, B. J. (2021). Data-driven resolvent analysis. *Journal of Fluid Mechanics*, *918*, A10.

Higdon, R. (2006). Numerical modelling of ocean circulation. *Acta Numerica*, *15*, 385 - 470. doi: 10.1017/S0962492906250013

Holland, W. R., & Lin, L. B. (1975). On the generation of mesoscale eddies and their contribution to the oceanicgeneral circulation. i. a preliminary numerical experiment. *Journal of Physical Oceanography*, *5*(4), 642–657.

Hu, Y., Chen, L., Wang, Z., & Li, H. (2022). Swinvrnn: A data-driven ensemble forecasting model via learned distribution perturbation. *Journal of Advances in Modeling Earth Systems*, *15*. doi: 10.1029/2022MS003211

Jayakumar, S. M., Czarnecki, W. M., Menick, J., Schwarz, J., Rae, J., Osindero, S., ... Pascanu, R. (2020). Multiplicative interactions and where to find them. In *International conference on learning representations.*

Jiang, C., Marcus, P., Xiao, H., Kashinath, K., Azizzadenesheli, K., Hassanzadeh, P., ... Esmaeilzadeh, S. (2021). Physics-informed machine learning: case studies for weather and climate modelling. *Philosophical Transactions of the Royal Society A*, *379*. doi: 10.1098/rsta.2020.0093

Jullien, S., Caillaud, M., Benshila, R., Bordois, L., Cambon, G., Dumas, F., ... Valat, S. A.-L. . S. (2025). Croco technical and numerical documentation. *Zenodo*. doi: https://doi.org/10.5281/zenodo.15064380

Keppler, R., Koch, J., & Fensholt, R. (2025). Learning 2d shallow water equations with physics-informed neural operator networks.

Kolář, V. (2007). Vortex identification: New requirements and limitations. *International Journal of Heat and Fluid Flow*, *28*(4), 638-652. Retrieved from `https://www.sciencedirect.com/science/article/pii/S0142727X07000343` (Including Special Issue of Conference on Modelling Fluid Flow (CMFF'06), Budapest) doi: https://doi.org/10.1016/j.ijheatfluidflow.2007.03.004

Kontolati, K., Goswami, S., Em Karniadakis, G., & Shields, M. D. (2024). Learning nonlinear operators in latent spaces for real-time predictions of complex dynamics in physical systems. *Nature Communications*, *15*(1), 5101.

Koopman, B. O. (1931). Hamiltonian systems and transformation in hilbert space. *Proceedings of the National Academy of Sciences*, *17*(5), 315–318.

Koopman, B. O., & Neumann, J. v. (1932). Dynamical systems of continuous spectra. *Proceedings of the National Academy of Sciences*, *18*(3), 255–263.

Li, Y., Sun, Q., Wei, J., & Huang, C. (2024). An improved pinn algorithm for shallow water equations driven by deep learning. *Symmetry*, *16*(10), 1376.

Lionst, J.-L., Temam, R., & Wan, S. (1992). On the equations of the large-scale ocean. *Nonlinearity*, *5*, 1007-1053. doi: 10.1088/0951-7715/5/5/002

Morrison, P. (1998). Hamiltonian description of the ideal fluid. *Reviews of Modern Physics*, *70*, 467-521. doi: 10.1103/revmodphys.70.467

Olver, P. J. (1993). *Applications of lie groups to differential equations* (Vol. 107). Springer Science & Business Media.

Ott, J., Pritchard, M., Best, N., Linstead, E. J., Curcic, M., & Baldi, P. (2020). A fortran-keras deep learning bridge for scientific computing. *Sci. Program.*, *2020*, 8888811:1-8888811:13. doi: 10.1155/2020/8888811

Pathak, J., Subramanian, S., Harrington, P., Raja, S., Chattopadhyay, A., Mardani, M., ... others (2022). Fourcastnet: A global data-driven high-resolution weather model using adaptive fourier neural operators. *arXiv preprint arXiv:2202.11214*.

Peixoto, P. S., & Schreiber, M. (2019). Semi-lagrangian exponential integration with application to the rotating shallow water equations. *SIAM Journal on Scientific Computing*, *41*(5), B903–B928.

Pond, S., & Bryan, K. (1976). Numerical models of the ocean circulation. *Reviews of Geophysics*, *14*, 243-263. doi: 10.1029/RG014I002P00243

Randall, D. A. (2011). An introduction to numerical modeling of the atmosphere. *Course Notes online at: http://kiwi. atmos. colostate. edu/group/dave/at604. html*.

Rosati, A., & Miyakoda, K. (1988). A general circulation model for upper ocean simulation. *Journal of Physical Oceanography*, *18*, 1601-1626. doi: 10.1175/1520-0485(1988)018⟨1601:AGCMFU⟩2.0.CO;2

Russkova, T. (2017). Performance analysis of a parallel monte carlo code for simulating solar radiative transfer in cloudy atmospheres using cuda-enabled nvidia gpu. In *23rd international symposium on atmospheric and ocean optics: Atmospheric physics* (Vol. 10466, pp. 311–321).

Schmid, P. J. (2010). Dynamic mode decomposition of numerical and experimental data. *Journal of fluid mechanics*, *656*, 5–28.

Sharma, A. S., Mezić, I., & McKeon, B. J. (2016). Correspondence between koopman mode decomposition, resolvent mode decomposition, and invariant solutions of the navier-stokes equations. *Physical Review Fluids*, *1*(3), 032402.

Shchepetkin, A. F., & McWilliams, J. C. (2009). Computational kernel algorithms for fine-scale, multiprocess, longtime oceanic simulations. In *Handbook of numerical analysis* (Vol. 14, pp. 121–183). Elsevier.

Soufflet, Y., Marchesiello, P., Lemarié, F., Jouanno, J., Capet, X., Debreu, L., & Benshila, R. (2016). On effective resolution in ocean models. *Ocean Modelling*, *98*, 36–50.

Stier, P., Dagon, K., Hall, D. M., Hoyer, S., Barnes, E. A., Yu, R., ... Barreiro, M. (2024). Pushing the frontiers in climate modelling and analysis with machine learning. *Nature Climate Change*. doi: 10.1038/s41558-024-02095-y

Wang, C., Pritchard, M. S., Brenowitz, N., Cohen, Y., Bonev, B., Kurth, T., ... Pathak, J. (2024). Coupled ocean-atmosphere dynamics in a machine learning earth system model. *arXiv preprint arXiv:2406.08632*.

Zhao, X.-z., Xu, T.-y., Ye, Z.-t., & Liu, W.-j. (2020). A tensorflow-based new high-performance computational framework for cfd. *Journal of Hydrodynamics*, *32*(4), 735–746.

Zhong, X., Ma, Z., Yao, Y., Xu, L., Wu, Y., & Wang, Z. (2023). Wrf–ml v1.0: a bridge between wrf v4.3 and machine learning parameterizations and its application to atmospheric radiative transfer. *Geoscientific Model Development*. doi: 10.5194/gmd-16-199-2023